Noname manuscript No.
(will be inserted by the editor)

Contributions of 3D printed fracture networks to development of flow and transport models

Anna Suzuki, James M. Minto, Noriaki Watanabe, Kewen, Li, · Roland N. Horne

Received: date / Accepted: date

Abstract Conventional experiments using natural rock samples have trouble in observing rock structures and controlling fracture properties. Taking advantage of 3D printing technologies, a complex fracture network was made by using a 3D printer. This approach allowed us to control the properties of the fracture networks and to prepare identical geometries for both simulation and experiment. A tracer response curve from the flow experiment was obtained and compared with numerical simulations. The result of the computational fluid dynamics (CFD) simulation based on the Navier-Stokes equations was in good agreement with experimental result, which suggested that the results of experiment and the CFD simulation are reliable. On the other hand, comparison with an equivalent permeability model based on the cubic law showed a discrepancy from the experimental result. This validation approach enabled

A. Suzuki
Tohoku University
2-1-1 Katahira, Aoba-ku, Sendai, Miyagi, 980-8577, Japan
Tel.: +81-22-217-5284
E-mail: anna.suzuki@tohoku.ac.jp

James M. Minto
University of Strathclyde 75 Montrose St, Glasgow G1 1XJ, UK
Tel.: +44 (0)141 548 3177
E-mail: james.minto@strath.ac.uk

Noriaki Watanabe
Tohoku University
468-1 Aramaki-Aza-Aoba, Aoba-ku, Sendai, Miyagi, 980-0845, Japan
Tel.: +81-22-795-7384
E-mail: noriaki.watanabe.e6 @tohoku.ac.jp

Kewen Li
Stanford University 367 Panama Street, Stanford, CA 94305, USA
E-mail: kewenli@stanford.edu

Roland N. Horne
Stanford University 367 Panama Street, Stanford, CA 94305, USA
E-mail: horne@stanford.edu

discussion of the limitation of the flow model. Because 3D printed fracture networks could reduce uncertainty between numerical simulation and laboratory experiment, they will be useful for understanding more detailed and more complicated phenomena in fracture networks.

Keywords fracture network; tracer experiment; CFD; equivalent permeability

1 Introduction

Fluid flow within fractured rocks is controlled by the fracture structures, however, detailed characterization of flow and transport processes within complex fracture networks remains challenging. Numerous studies have investigated flow behavior in single fractures at local scale. The single fractures have traditionally been idealized as a set of parallel plates to yield the well-known cubic law (Snow 1965; Witherspoon et al. 1980; Zimmerman and Bodvarsson 1996). The cubic law is the simplest model of flow through a rock fracture that removes the nonlinear term from the Navier-Stokes equation. Several flow experiments through single fractures using two rough-walls have been reported (Hakami and Larsson 1996; Yeo et al. 1998; Konzuk and Kueper et al. 2004; Sawada and Sato 2010; Al-Yaarubi et al. 2005; Tzelepis et al. 2015). They measured the roughness of the fracture surface and obtained the accurate two-dimensional aperture data. The aperture data were used to calculate the permeability and the flow in the fractures based on the local cubic law. Comparison between the experimental results and the calculation revealed that for the rough-wall fractures the flow rates from the aperture data were overestimated by around 1.2-2.5 times the experimental flow rates. The accurate aperture data were also used to conduct flow simulation by using the Navier-Stokes equations. These approaches, i.e., comparing theories, experiments, and simulations using the same geometry data, clarified the applicability and/or the insufficiency of the cubic law and could provide deep understanding of interactions between flow and structures in fractured rocks.

In nature, multiple fractures constitute three-dimensional networks. The networks can be complex due to anisotropy and wide variations of fracture properties. Fractures themselves have complex shapes (e.g., roughness), and their intersections and connections with other fractures also lead to complex flow. Combining these complex factors and simulating multiphysical behaviors make computation costs extremely expensive. For this reason, elaborate flow simulations are unrealistic for fracture networks.

At large scale, flow in fractured rocks has often been simulated by discrete fracture network models (DFNs) (Long et al. 1982; Cacas et al. 1990; Jing 2003; Erhel et al 2009; Dershowitz et al. 1999; Hyman et al. 2015). In the DFNs, fluid flow in individual fractures was assumed to obey the cubic law. (Min and Jing 2003; Javadi et al. 2010; Adler et al. 2013; Liu et al. 2016). Liu et al. (2016) reviewed the important factors for estimation of equivalent permeability in the DFNs and concluded that, although many efforts have been

Table 1 Material properties for printed specimens and fracture network properties.

Matrial Properties	Value
Composition	UV Curable Acrylic Plastic
Density @ 80 deg C (liquid)	1.02 g/cm3
Tensile Strength	42.4 MPa
Tensile Modulus	1283 MPa
Elongation at Break	6.83 %
Flexural Modulus	1159 MPa
Sample size	ϕ 1 inch x 4 cm height
Fracture length	3.2 14.9 mm
Fracture aperture	0.2 0.932 mm
Aperture ratio (thickness/length)	0.0625
Orientation	random
Position	2.5 kJ/m2

devoted, difficulties in modeling flow in fractures due to complex geometries and mechanical and hydraulic environment have encumbered the DFN's broad application.

Because of the ability to control the internal structure, 3D printing technologies are expected to play a role linking flow models and experiments for fracture networks. Several researches have explored the potential of using 3D printing in geological studies (e.g., Ishutov et al. 2015; Head et al. 2016). This study proposed a validation method for flow models in which the same synthetic fracture network geometry is both modeled numerically and 3D printed for flow experiments, with the aim of allowing discussion on the applicability and/or the limitations of the flow models in complex fracture networks.

2 3D printed fracture network

Suzuki et al. (2017) created a fracture network model with a 3D printer. The details of the fracture network model creation can be found in Suzuki et al. (2017). Disc-shaped fractures were distributed randomly and evenly in the whole domain with the range of fracture length between 3.2 mm and 14.9 mm, as shown in Fig. 1(a). The number of fractures was determined according to a power-law scaling. The aperture was proportional to the length, which was in the range between 0.2 mm and 0.932 mm. The sizes of fractures were determined by the capability of the 3D printer. The parameters of the fracture network are listed in Table 1. The cluster of fractures shown in Fig. 1(a) were subtracted from a solid cylinder to create the fracture network (Fig. 1(b)) 4 cm in height and 2.54 cm in diameter.

The fracture network model was converted to a STL file and sent to a 3D printer. The 3D printer used in this study was the ProJet HD 3000Plus (3D Systems) incorporating the multijet modeling (MJM) method. The MJM is a rapid prototyping process that provides a quick turnaround for smooth, high-resolution, hard plastic parts with complex geometries. The base material used

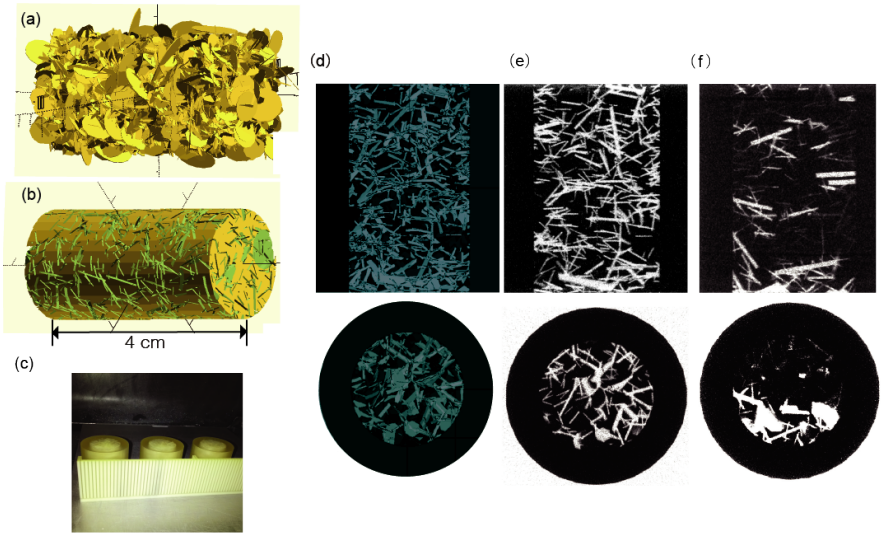

Fig. 1 Creating 3D printed fracture network. (a) Distributions of disc-shaped fractures, (b) Sample design (Green parts are fractures.), (c) photo during printing, (d) cross sectional image of the original, (e)(f) cross sectional images of CT scan of the printed sample. The sample was treated (e) with hexane and (f) with ethanol to remove wax (Suzuki et al. 2017).

in this study was UV curable acrylic plastic (VisiJet EX200 Plastic Material), solidified by UV lamps.

The 3D printer required removal of the wax from the inside of the sample after printing. The cross-sectional image of the original design is shown in Fig. 1(d), and the cross-sectional CT scanning images of samples treated with two different methods of wax removal are shown: Fig. 1(e) where hexane was used to remove wax, and 1(f) where ethanol was used. The optical porosity determined from the micro-CT scan was 40.5 % for the sample treated with hexane, which was almost same as the value of 40.2 % for the computational design. The sample treated with hexane removed wax well enough and so was used in the experimental part of this study.

3 Tracer test

The configuration of the apparatus for the tracer transport experiment is shown in Fig. 2. Before the flow experiment, the sample was immersed in water under vacuum for full saturation for more than one day. The water was injected into the samples by constant hydraulic head difference. Platens with spider web patterns for flow distribution were used at the inlet and the outlet to ensure homogeneous spatial distributions of injected water. In order to examine dependence of flow rate, the elevation of the water source was set successively to 28, 56, and 114 cm. The discharge per unit area was obtained by weighing the water outflow.

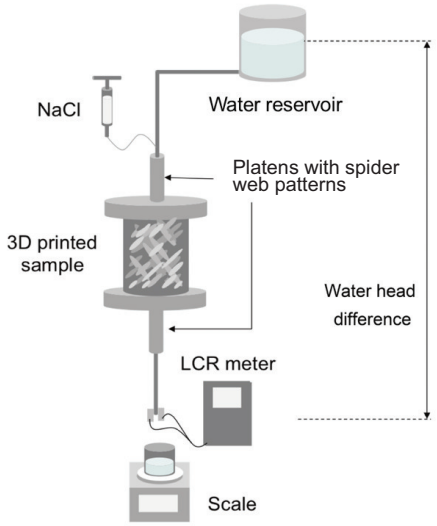

Fig. 2 Configuration of the experimental apparatus

Saline solution was used as a conservative tracer. Electric resistivity was measured over time at the outlet by using a DE-6000 LCR meter. The values of electric resistivity could be converted to tracer concentration that had a linear relationship with the electrical conductivity. All electric resistivity was measured at the outlet using alligator clips that were set at the same distance to eliminate geometrical factors. Once the resistivity was stabilized, 2 milliliters of 5 %wt salt water was injected by a syringe from the inlet. In order to compare with simulations, the obtained tracer response was normalized by the injected concentration (5 %wt).

4 Numerical simulation

4.1 Model in OpenFOAM

The CFD software OpenFOAM (www.openfoam.org) was used to solve fluid flow with the Navier-Stokes equations and tracer transport with the advection-dispersion equation. Model geometry was defined by the same STL file sent to the 3D printer, with the addition of inlet and outlet caps to facilitate flow distribution. The fracture network was discretized into 23.6 million mostly hexahedral cells with average cell size of 64 μm using the mesh generation tool snappyHexMesh, as shown in Fig. 3. The main input parameters of the OpenFOAM model are listed in Table 2. First, the Navier-Stokes solver named simpleFoam was used to calculate the steady-state flow field, with flow driven by a specified constant flow rate inlet boundary condition and specified constant pressure outlet boundary condition. No-flow conditions were used at the side boundaries. Then the transport of a conservative tracer was simulated

Table 2 Simulation parameters in OpenFOAM.

Parameter	Value
Number of cells	$23,596,963$
Flow rate [m^3/s]	1.75×10^{-7}
Fluid viscosity [Pa·s]	9.32×10^{-4}
Fluid density [kg/m^3]	997.5
Dispersivity [m^2/s]	1.0×10^{-9}
Tracer concentration [-]	1
Tracer volume [mL]	2

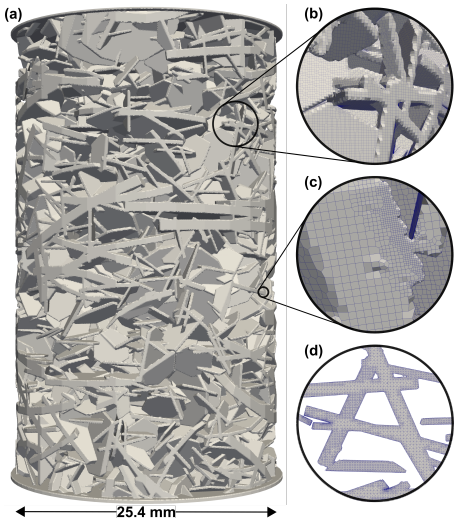

Fig. 3 3D discrete fracture network in OpenFOAM. (a) modeled domain with inlet (top) and outlet (bottom), (b)(c) close-up with cells and cell refinement visible, (d) cross-section through complex fracture intersections showing the internal arrangement of cells.

with a custom advection-dispersion solver using the flow field already calculated.

4.2 Equivalent permeability model

CFD software such as OpenFOAM could simulate detailed flow with the same STL file used in the 3D printer. However, solution of the Navier-Stokes equations in this manner required a large computational mesh that was both time-consuming to generate and to optimize the constitutive parameters, as well as limited in size and resolution by the amount of RAM available. On the other hand, when developing at actual field scales, it was impossible to capture all the detailed structures and to output statistics such as in Monte Carlo simulations without incurring extremely high computational costs. Thus, a simulation was required that produces reasonable results by a simplified method (e.g., homogenization). There were well-known methods of converting information of

fractures and calculating equivalent permeability in discrete fracture network models (e.g., see review by Liu et al. (2016)). The simulation and the experimental results were compared to discuss the applicability and the limitation of the flow model.

By neglecting inertial forces in the fluid, the Navier-Stokes equations could be reduced to the linear Stokes equation (i.e., Poiseuille flow). The cubic law has been known as the solution of the linear Stokes equations under a uniform one-dimensional pressure gradient between two smooth parallel plates with a parabolic velocity distribution across the fracture aperture (Lomize 1961; Snow 1965; Louis 1969; Krantz et al. 1979; Tsang and Witherspoon 1981; Zimmerman and Bodvarsson 1996):

$$Q = \frac{wb^3}{12\mu}\nabla P = \frac{KA}{\mu}\nabla P \tag{1}$$

where Q is the total volumetric flow rate through fractures, w is the fracture width (perpendicular to the pressure gradient) and b is the fracture aperture, μ is the viscosity of water, ∇P is the pressure gradient, K is the fracture permeability and A is the cross-sectional area.

The domain of the fracture network was divided into lattice grids and extracted the fracture length and the fracture aperture of fractures crossing the grids. From the fracture width and the fracture aperture of all the fractures intersecting each grid, the "equivalent" permeability at each lattice plane was calculated by the following form (Watanabe and Takahashi 1995; Jing et al. 2000; Ishibashi et al. 2012):

$$K_x = \sum_j \frac{b_j^3 w_j}{12A_x}, K_y = \sum_j \frac{b_j^3 w_j}{12A_y}, K_z = \sum_j \frac{b_j^3 w_j}{12A_z} \tag{2}$$

where A_x, A_y, A_z are the areas of grid cell interfaces orthogonal to the x, y, and z axis, respectively. All fractures crossing at each interface of grid cell are numbered in j. The aperture and the width of the fracture intersecting the interface of grid cells are written as b_j and w_j.

Equivalent permeability on each grid surface obtained was substituted into the following conservation of mass equation for incompressible fluid:

$$\frac{\partial}{\partial x}(\frac{K_x A_x}{\mu}\frac{\partial P}{\partial x}) + \frac{\partial}{\partial y}(\frac{K_y A_y}{\mu}\frac{\partial P}{\partial y}) + (\frac{\partial}{\partial z}\frac{K_z A_z}{\mu}\frac{\partial P}{\partial z}) = 0. \tag{3}$$

In this study, incompressible, single-phase flows were considered. The density of rock and water, the viscosity of water, and the porosity were assumed constant. Constant pressure conditions were given at the upstream and the downstream boundaries. The gravitational force were given in the vertical direction. No-flow conditions were used at the side boundaries. The finite difference equation of Eq. (3) was solved numerically by the incomplete Cholesky conjugate gradient (ICCG) method. Ten thousand tracer particles were injected as a pulse from the upstream boundary. A tracer particle migrated from a grid cell to its adjacent grid cell until the particle reached the downstream boundary.

The travel direction of tracers was determined by a probability that depends on the magnitude of the flow rate given by Eq. (1). A plot of the number of tracer particles crossing the downstream boundary over time was used as a tracer response curve.

5 Experimental results

Before the flow test, Suzuki et al. (2017) measured the pore volume of the 3D printed sample and confirmed the value was close to the value obtained from the known geometry (5273.18 mm^3 from the experiment and 5957 mm^3 from the CT scanner.)

The optical porosities were 40.5 % for the sample treated with hexane and 40.2 % for the computational design. It should be mentioned that, due to the complexity of the fracture network, the porosities were far larger than the values normally used in reservoir simulations of fractured rocks. Although the porosity of the sample was larger than that of natural rocks, the aim in this study was not to create fracture structures replicating natural rocks, but to compare the flow models and the flow experiment in a challengingly complex fracture network. Additionally, as the base material of the sample was acrylic plastic, unlike natural rocks, the matrix had zero permeability resulting in no fluid flow unless fractures were connected.

The flow test was repeated three times with different hydraulic heads (h = 28, 56, and 114 cm). The weight of water at the outlet was measured to calculate the volumetric discharge per unit area. The discharge per unit areas with different hydraulic heads were 0.03, 0.07, and 0.14 cm/s, respectively. The correlation between discharge per unit areas and the hydraulic heads is shown in Fig. 4. As shown in Fig. , the correlation was approximated by a line with zero intercept. (The determination coefficient was 0.99.) The linear correlation indicated that the experimental results were in the range of the Darcys law. Based on Darcy's law, the permeabilities for the whole sample were obtained as 4.7×10^{-12}, 5.0×10^{-12}, and 4.6×10^{-12} m^2 for the three different hydraulic heads. As similar values of permeability were obtained at different hydraulic heads, this setup was considered acceptable. Reynolds number was calculated as (Qian et al. 2005; Tzelepis et al. 2015):

$$Re = \frac{\rho R V}{\mu} = \frac{V b}{2\nu} \tag{4}$$

where ρ is the density of water $[kg/m^3]$, and R is the hydraulic radius [m], which is approximated by the relation $R \approx b/2$ (Tzelepis et al. 2015).

In this study, Re ranged over 0.04-0.19, 0.08-0.40, and 0.15-0.73 by substituting the range of apertures for the discharge per unit areas of 0.03, 0.07, and 0.14 cm/s, respectively. The inertial force was negligible at sufficiently small values of Re ($Re < 1$), in which flow was described by Darcy's law (Schrauf and Evans 1986; Zimmerman and Bodvarsson 1996; Brush and Thomson 2003). Several criteria have been argued when the inertial forces begin to affect the

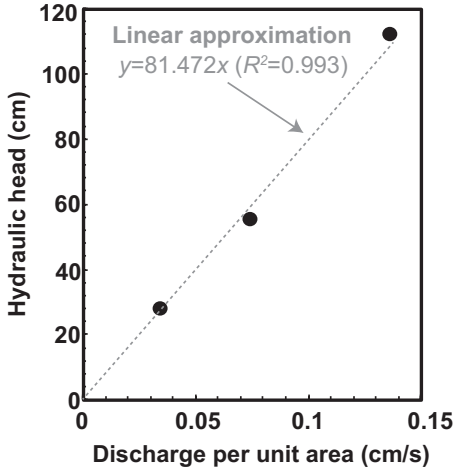

Fig. 4 Correlation between flow rate and pressure gradient from the experimental results.

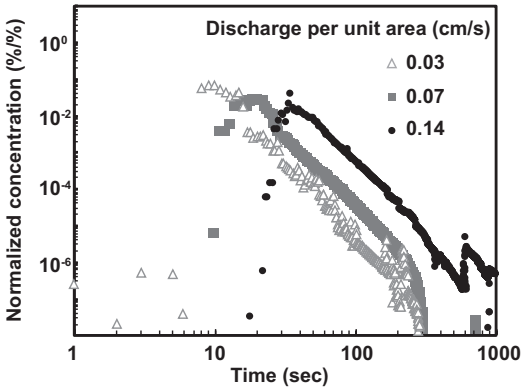

Fig. 5 Tracer response curves using 3D printed fracture network model.

flow behaviors (e.g., Re of about 15, Zimmerman and Yeo 2000). The values of Re in this study were smaller than those criteria, which indicated that the flow was sufficiently slow and the inertia effect was negligible.

The experimental tracer responses for different hydraulic heads are plotted in Fig. 5. The three responses showed power-law declines in the later stages. These power-law declines were considered to be caused by the wide range of fracture apertures in the fracture network model (Suzuki et al. 2016). When the flow rate was small, the tracer response was delayed.

6 Simulation results

The experimental result for the discharge per unit area of 0.03 cm/s ($0.04 < Re < 0.19$) was compared with numerical simulations. Because $Re < 1$, the cubic law should be guaranteed. The same condition was set as the flow experiment in the simulation models.

6.1 Results from OpenFOAM

The OpenFOAM numerical model results were interpreted in terms of pressure distribution, velocity field (with associated stream lines) and tracer transport. Pressure distribution is shown in Figs. 6(e). The outlet pressure was set at zero whilst the inlet pressure and the pressure distribution throughout the fracture network were calculated from the Navier-Stokes equations for the specified flow rate. The pressure distribution decreased gradually from the inlet to the outlet and there seemed to be no location where excessive pressure was applied. Units for pressure were given as m^2/s^2 due to the use of an incompressible solver in which the Navier-Stokes equations have been normalized by fluid density to improve computational efficiency.

The cross-sections of the velocity field in the fracture network was shown in Fig. 6(a-d). It was observed that large aperture fractures generally had higher velocity than small aperture fractures as shown in Fig. 6(a-d). The areas with highest velocity tended to be in the center of the large aperture fractures, or at fracture intersections where pathways combined. On the other hand, some small aperture fractures had fast flow velocity. It appeared that all alternative flow paths around these small fractures were less well connected and so were less preferential, hence the flow became concentrated and these particular small aperture fractures might behave as bottlenecks restricting flow through the fracture network. These observations demonstrated the importance of the structure and connectivity of the fracture network on fluid transport.

The stream lines in the fracture network is shown in Fig. 7(a), calculated using a Runge-Kutta algorithm in the visualization software ParaView (Ahrens et al. 2015) applied to the OpenFOAM calculated velocity field. Streamlines originated at the inlet and extend towards the outlet, progressively converging along the way, or terminating when their velocity drops below a threshold (arbitrarily set at 1×10^{-6} m/s). In this way, the streamlines delineated the preferential flow pathways, also known as the hydraulic backbone.

Tracer transport calculated using an advection-dispersion equation is plotted as time to arrival in Fig. 7(b-f): the first time at which tracer concentration in each cell exceeded 1% of the inlet tracer concentration. In the 3D volume view of Fig. 7(b), regions of the fracture network in which tracer concentration did not exceed 1% of the inlet concentration at the point of tracer breakthrough (11 s) were rendered transparent (see supporting information for an animation of tracer time to arrival). The cross sections of Fig. 7(c-f) show tracer time to

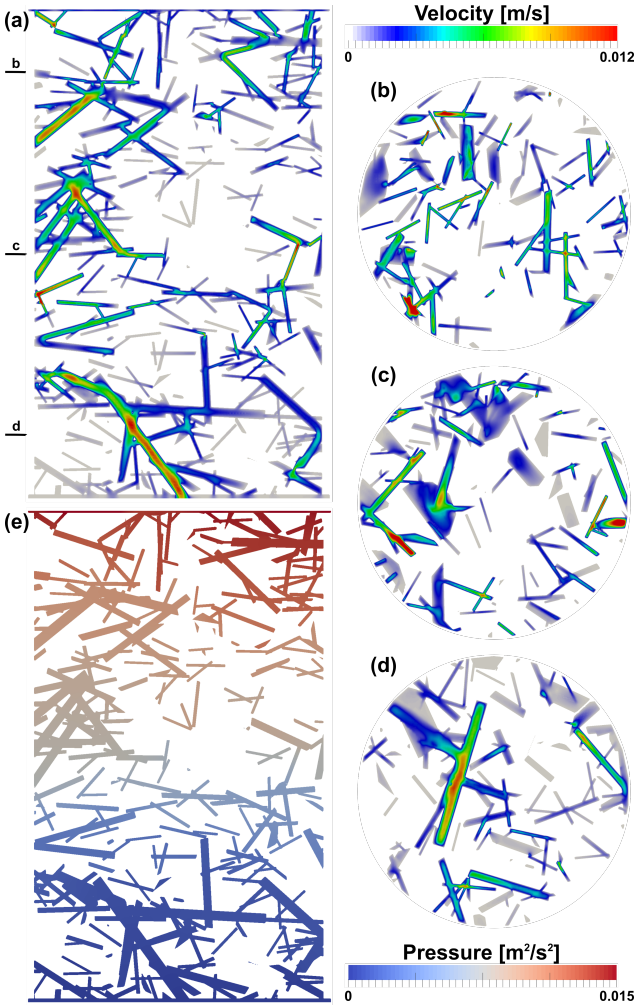

Fig. 6 Results of OpenFOAM simulation. (a) velocity distribution in vertical section and in (b)(c)(d) cross sections, (e) pressure distribution (N.B. pressure normalized by fluid density, as standard for incompressible fluid solvers, hence pressure units of m^2/s^2).

arrival with areas where tracer concentration never exceeded 1% over the 162 sec model duration rendered in black.

Tracer transport paths resembled those of the streamlines: at the inlet there were many flow paths entering the network, while limited paths could be observed around the outlet implying that paths converged along the way. The trend of transport paths was similar to flow in natural river catchments where upstream tributaries gathered and eventually became a main channel. The result suggested that a complicated structure did not create priority flow paths from the beginning, but it was the progressive convergence of pathways that left only preferential flow paths at the outlet. It should be borne in mind

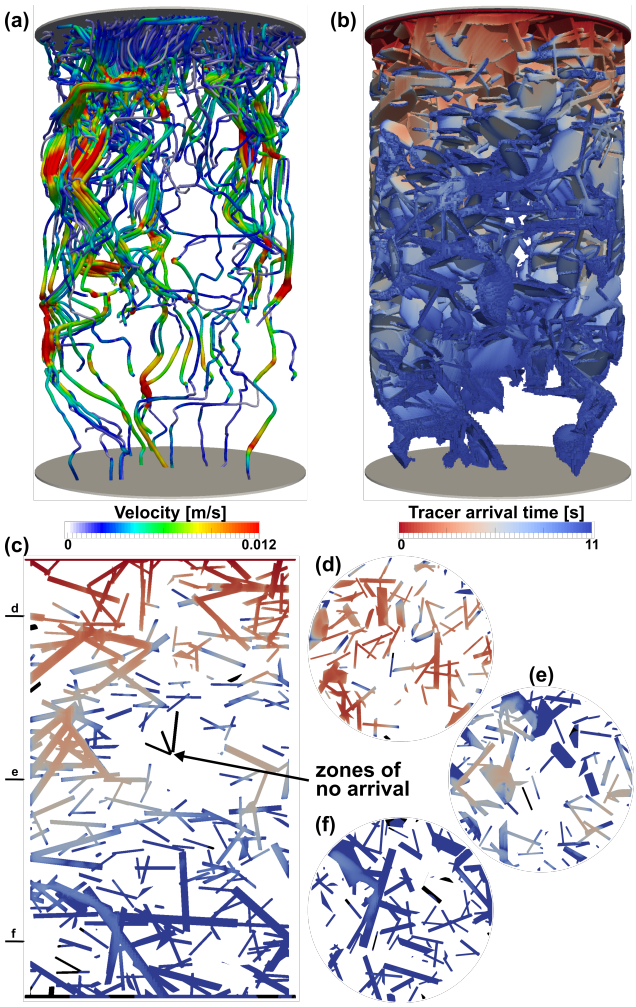

Fig. 7 (a) flow stream lines, (b-f) time required for tracer concentration to exceed 1% of inlet concentration. In (c-f), regions of the fracture network in which tracer concentration never exceeds 1% are shown in black and labeled as zones of no arrival.

that this observation might be the result of the boundary conditions imposed on both the physical tracer experiment and the numerical simulation whereby tracer was distributed uniformly across the inlet. Even though the fractures were distributed randomly and evenly throughout the entire volume, there appeared to be an area in the center that did not contribute to tracer transport and which might have therefore contributed to the formation of preferential flow paths.

The experimental tracer response was compared to the modeled amount of tracer passing through the outlet boundary (Fig. 8). To allow a direct comparison, it was necessary to normalize the simulated tracer to the experimental

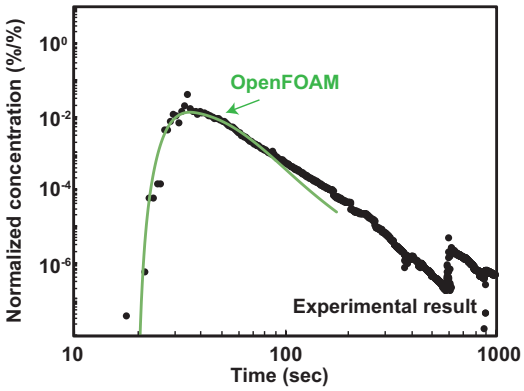

Fig. 8 Comparison between simulation result from OpenFOAM and experimental result.

tracer range; this was done by matching the area of the response curve. The OpenFOAM model simulated flow in the fracture network, but not in the tube from the injection point to the fracture network model, nor from the fracture network model to the LCR meter. Thus, The offset of 13.5 sec was set to fit the experimental response. The normalized response data is in good agreement with the experimental results. Although The simulation was stopped at 162 sec (at 99.9% tracer recovery), A power-law decline was observed on the tail, which was consistent with the experimental result. The power-law decline suggested that by solving the Navier-Stokes and advection-dispersion equations, complex flow behavior in fracture networks could be simulated, provided the STL file of the structure and its suitably fine mesh were prepared.

6.2 Results from equivalent permeability model

The tracer response was compared with the numerical result from the equivalent permeability model, as plotted in Fig. 9. The same offset of 13.5 sec was used as in the OpenFOAM model. First, permeability was calculated, and flow and transport were simulated based on the cubic law. The result was shown as the dashed line ($\eta = 1$) in Fig. 8, which was an earlier response than the experimental result. This discrepancy suggested that the model overestimated the permeability and the flow rate.

Numerous studies have discussed the discrepancy between flow rates measured experimentally and the simulated results from the cubic law (e.g., Konzuk et al. 2004). The errors might be introduced due to experimental flow condition (Hakami and Larsson 1996) and definition of apertures (Mourzenko et al. 1995; Ge 1997; Oron and Berkowitz 1998; Brush and Thomson 2003) and so on. Various modifications of the cubic law have been proposed, and the most popular approach has been to modify the definition of the aperture used in their equations (see, e.g., Smith and Freeze 1979; Tsang and Witherspoon

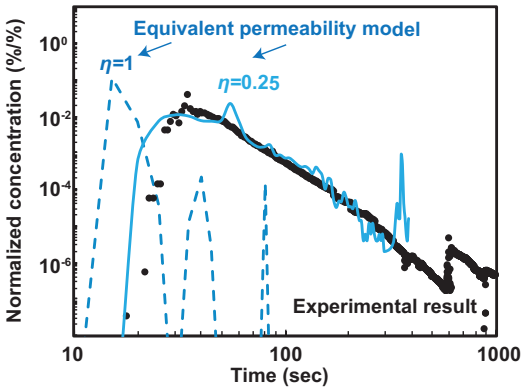

Fig. 9 Comparison between simulation result from equivalent permeability model and experimental result.

1981; Neuzil and Tracy 1981; Tsang 1984; Brown 1987; Hakami and Barton 1990; Tsang and Tsang 1990; Zimmerman et al. 1991; Unger and Mase 1993; Renshaw 1995).

To adjust the overestimation, effective aperture was introduced given by $b' = \eta b$ where η is the factor and b is the aperture in the original fracture network model. The model results with $\eta = 0.25$ was plotted by the solid line. The parameter η less than 1 meant the effective aperture was narrower than the original aperture. The result with $\eta = 0.25$ showed a later response than that with $\eta = 1$. When $\eta = 0.25$, the result was closer to the experimental result.

If the 3D printer created fractures with the effective apertures, the printed fracture apertures would be 0.25 of the original sizes. On the other hand, comparison with the CT scan images (Suzuki et al. 2017) indicated that the 3D printer resolution was sufficient to reproduce the fracture network. In addition, the result of the OpenFOAM model showed that the CFD type of model can reproduce the tracer response. From these points, the discrepancy appeared to come from the modeling flows in the equivalent permeability model. Because the fracture apertures were allocated from fracture information, the equivalent permeability model did not consider the change in the aperture due to inclination, which might lead to overestimation of flow rates (Mourzenko et al. 1995; Ge 1997; Oron and Berkowitz 1998; Brush and Thomson 2003). In addition, the model determined the tracer migration due to the probability of magnitude of flow rate. This simulation method for tracer migration might also produce a deviation from the actual behavior. Although the flow in this study was in the laminar flow regime at low Reynolds number, in which inertial effects at intersections were negligible (Wilson and Witherspoon 1976), complex networks may enhance the physical mixing (Johnson et al. 2006; Kang et

al 2015; Bernabè et al. 2016). To understand this complexity, future studies could use simpler geometries.

The 3D printer used plastic as the base material, which differed from natural rocks in terms of internal compositions and chemical and physical reactions on the surfaces. However, the influence of geometries could be examined not only for single-phase but also for multiphase flow. This verification could not be achieved easily with natural rock samples so far. Thus, the validation with 3D printed fracture networks will be of great help to understand flow behaviors in fracture networks.

7 Conclusion

This study proposed a new method to validate and to analyze flow models for fracture networks. A complex fracture network was made by using a 3D printer and conducted flow tests. The experimental result and the computational fluid dynamics (CFD) simulation result were consistent with each other. Their results were considered reliable. The CFD simulation revealed how complicated flows were formed in the fracture network. Although the CFD had a very high computational cost and the equivalent permeability model was expected to reduce the cost, comparison with the equivalent permeability model showed a discrepancy from the experimental result. The results indicated that the discrepancy came from the limitations of the equivalent permeability model.

3D printers allow us to create the fracture geometry of either actual distributions (i.e. CT scan images or outcrop photos) or any type of geometric models (i.e. geometric network or stochastic heterogeneity of petrophysical properties) repeatedly. Although this study only focused on simulation of flow and transport, the same approach of analysis and comparison between theoretical models and their simulations are expected to extend to multiphysical behaviors (e.g. contamination, precipitation, thermal effect, etc.). Experiments using 3D printed fractures will be a useful approach that fills the conventional gaps between modeling and laboratory experiments.

8 Acknowledgements

This work was supported by the Japan Society for the Promotion of Science under Grant-in-Aid for Young Scientists(A)(JP17H04976) and under Grant-in-Aid for Challenging Research (Exploratory)(JP17K19084) and Engineering and Physical Sciences Research Council (EPSRC) Bright IDEAS award: The Big Pitch (grant number EP/M016854/1), whose supports are gratefully acknowledged. Requests for numerical and experimental data should be addressed to Anna Suzuki (e-mail: anna.suzuki@tohoku.ac.jp).

References

1. Adler, P.M., Malevich, A.E., Mityushev, V.V.: Nonlinear correction to Darcys law for channels with wavy walls. Acta Mech. 224(8), 1823–1848 (2013). https://doi.org/10.1007/s00707-013-0840-3
2. Ahrens, J., Berk, G., Law, C.: ParaView: an end-user tool for large data visualization. In: Hansen, C.D., Johnson, C.R. (Ed.) Visualization Handbook, pp. 717-732 (2005). http://www.paraview.org
3. Al-Yaarubi, A.H., Pain, C.C., Grattoni, C.A., Zimmerman, R.: NavierStokes simulations of fluid flow through a rock fracture. In: Faybishenko (Ed.), Dynamics of Fluids and Transport in Fractured Rock. AGU, pp. 55-64 (2005)
4. Bear, J.: Dynamics of fluids in porous media. American Elsevier, New York (1972)
5. Bernabè Y, Wang Y, Qi T, Li M.: Passive advection-dispersion in networks of pipes: effect of connectivity and relationship to permeability. J. Geophys. Res. Solid Earth (1978 2012) 121, 713-728 (2016). https://doi.org/10.1002/2015 JB012487
6. Brown, S.R.: Fluid flow through rock joints: the effect of surface roughness. J. Geophys. Res. Solid Earth (1978-2012) 92(B2), 1337-1347 (1987). https://doi.org/10.1029/JB092iB02p01337
7. Brush, D.J., Thomson, N.R.: Fluid flow in synthetic rough-walled fractures: Navier-Stokes, Stokes, and local cubic law simulations. Water Resour. Res. 39(4), 1085 (2003). https://doi.org/10.1029/2002WR001346
8. Cacas, M.C., Ledoux, E., Marsily, G., Tillie, B., Barbreau, A., Durand, E., Feuga, B., Peaudecerf, P.: Modeling fracture flow with a stochastic discrete fracture network: calibration and validation - 1, the flow model. Water Resour. Res. 26(3), 479-489 (1990). https://doi.org/10.1029/WR026i003p00479
9. Dershowitz, W.S., Fidelibus, C.: Derivation of equivalent pipe network analogues for three-dimensional discrete fracture networks by the boundary element method. Water Resour. Res. 35(9), 2685–2691 (1999). https://doi.org/10.1029/1999WR900118
10. Erhel, J., De-Dreuzy, J.R., Poirriez, B.: Flow simulation in three-dimensional discrete fracture networks. SIAM J. Sci. Comput. 31(4), 2688-2705 (2009). https://doi.org/10.1137/080729244
11. Ge, S.: A governing equation for fluid flow in rough fractures. Water Resour. Res. 33(1), 53-61 (1997). https://doi.org/10.1029/96WR02588
12. Hakami, E., Larsson, E.: Aperture measurements and flow experiments on a single natural fracture. Int. J. Rock Mech. Min. Sci. Geomech. Abstr. 33(4), 395-404 (1996). https://doi.org/10.1016/0148-9062(95)00070-4
13. Hakami, E., Barton, N.: Aperture measurements and flow experiments using transparent replicas of rock joints, In: Barton, N., Stephansson, O. (Ed.), Rock Joints, pp. 383-390, Balkema, Brookfield (1990)
14. Head, D., Vanorio, T.: Effects of changes in rock microstructures on permeability: 3-D printing investigation. Geophys. Res. Lett. 43, 7494-7502 (2016). https://doi.org/10.1002/2016GL069334
15. Hyman, J.D., Karra, S., Makedonska, N., Gable, C.W., Painter, S.L., Viswanathan, H.S.: DFNWORKS: A discrete fracture network framework for modeling subsurface flow and transport. Comput. Geosci. 84, 10–19 (2015). https://doi.org/10.1016/j.cageo.2015.08.001
16. Ishibashi, T., Watanabe, N., Hirano, N., Okamoto, A., Tsuchiya, N.: GeoFlow: a novel model simulator for prediction of the 3-D channeling flow in a rock fracture network. Water Resour. Res. 48(7), W07601 (2012). https:// doi.org/10.1029/2011WR011226
17. Ishutov, S., Hasiuk, F.J., Harding, C., Gray, J.N.: 3D printing sandstone porosity models, Interpreation 3(3), SX49-SX61 (2015). https://doi.org/10.1190/INT-2014-0266.1
18. Javadi, M., Sharifzadeh, M., Shahriar, K.: A new geometrical model for non-linear fluid flow through rough fractures. J. Hydrol. 389(1), 18-30 (2010). https://doi.org/10.1016/j.jhydrol.2010.05.010
19. Jiang, Q., Feng, X., Song, L., Gong, Y., Zheng, H., Cui, J.: Modeling rock specimens through 3D printing: Tentative experiments and prospects. Acta Mech. Sin. 32(1), 101-111 (2016). https://doi.org/10.1007/s10409-015-0524-4
20. Jing, Z., Richards, J.W., Watanabe, K., Hashida, T.: A three-dimensional stochastic rock mechanics model of engineered geothermal systems in fractured crystalline rock. J. Geophys. Res. 105(B10), 23,663-679 (2000). https://doi.org/10.1029/2000JB900202

21. Ju, Y., Xie, H., Zheng, Z., Lu, J., Mao, L., Gao, F., Peng, R.: Visualization of the complex structure and stress field inside rock by means of 3D printing technology. Chin. Sci. Bull. 59(36), 5354-5365 (2014). https://doi.org/10.1007/s11434-014-0579-9
22. Johnson, J., Brown, S., Stockman, H.: Fluid flow and mixing in rough-walled fracture intersections. J. Geophys. Res. Solid Earth (1978-2012) 111(B12), (2006). https://doi.org/10.1029/2005JB004087
23. Kang, P.K., Dentz, M., Borgne, T.L., Juanes, R.: Anomalous transport on regular fracture networks: impact of conductivity heterogeneity and mixing at fracture intersections. Phys. Rev. E 92(2), 022148 (2015). https://doi.org/10.1103/PhysRevE.92.022148
24. Konzuk, J.S., Kueper, B.H.: Evaluation of cubic law based models describing single-phase flow through a rough walled fracture. Water Resour. Res. 40(2), W02402 (2004). https://doi.org/10.1029/2003WR002356
25. Liu, R., Li, B., Jiang, Y., Huang, N.: Review: Mathematical expressions for estimating equivalent permeability of rock fracture networks. Hydrogeol. J. 24, 1623-1649 (2016). https://doi.org/10.1007/s10040-016-1441-8
26. Long, J.C.S., Remer, J.S., Wilson, C.R., Witherspoon, P.A.: Porous media equivalents for networks of discontinuous fractures. Water Resour. Res. 18(3), 645–658 (1982). https://doi.org/10.1029/WR018i003p00645
27. Luo, J., Zhu, Y., Guo, Q., Tan, L., Zhuang, Y., Liu, M., Zhang, C., Xiang, W., Rohn, J.: Experimental investigation of the hydraulic and heat-transfer properties of artificially fractured granite. Sci. Rep. 7, 39882 (2017). https://doi.org/10.1038/srep39882
28. Min, K.B., Jing, L.: Numerical determination of the equivalent elastic compliance tensor for fractured rock masses using the distinct element method. Int. J. Rock Mech. Min. Sci. 40(6), 795–816 (2003). https://doi.org/10.1016/S1365-1609(03)00038-8
29. Mourzenko, V.V., Thovert, J.-F., Adler, P.M.: Permeability of a single fracture: Validity of the Reynolds equation. J. Phys. II Paris, 5, 465-482 (1995)
30. Neuzil, C.E., Tracy, J.V.: Flow through fractures. Water Resour. Res. 17(1), 191-199 (1981). https://doi.org/10.1029/WR017i001p00191
31. Oron, A.P., Berkowitz, B.: Flow in rock fractures: The local cubic law assumption reexamined. Water Resour. Res. 34(11), 2811-2825 (1998). https://doi.org/10.1029/98WR02285
32. Persoff, P., Pruess, K., Myer, L.: Two-phase flow visualization and relative permeability measurement in transparent replicas of rough- walled rock fractures. Proc. 16th Workshop on Geothermal Reservoir Engineering, Stanford University, Stanford, California, January 23-25 (1991)
33. Renshaw, C.E.: On the relationship between mechanical and hydraulic apertures in rough-walled fractures. J. Geophys. Res. Solid Earth (19782012) 100(B12), 24629-24636 (1995). https://doi.org/10.1016/j. enggeo.2013.05.013
34. Schrauf, T.W., Evans, D.D.: Laboratory studies of gas flow through a single natural fracture. Water Resour. Res. 22(7), 1038-1050 (1986). https://doi.org/10.1029/WR022i007p01038
35. Sawada, A., Sato, H.: A study of hydraulic properties in a single fracture with in-plane heterogeneity: an evaluation using optical measurements of a transparent replica. NET 42(1), 9-16 (2010)
36. Smith, L., Freeze, R.A.: Stochastic analysis of steady state groundwater flow in a bounded domain: 2. two-dimensional simulations. Water Resour. Res. 15(6), 1543-1559 (1979). https://doi.org/10.1029/WR015i006p01543
37. Snow, D.T.: A parallel plate model of fractured permeable media. PhD Thesis Univ. of Calif., Berkeley, USA (1965)
38. Suzuki, A., Niibori, Y., Fomin, S.A., Chugunov, V.A., Hashida, T.: Fractional derivative-based tracer analysis method for the characterization of mass transport in fractured geothermal reservoirs. Geothermics 53, 125-132 (2015). https://doi.org/10.1016/j.geothermics.2014.05.003
39. Suzuki, A., Watanabe, N., Li, K., Horne, R.N.: Fracture network created by 3D printer and its validation using CT images, Water Resour. Res. 53, 6330–6339 (2017). https://doi.org/10.1002/2017WR021032
40. Tsang, Y.W.: The effect of tortuosity on fluid flow through a single fracture. Water Resour. Res. 20(9), 1209-1215 (1984). https://doi.org/10.1029/WR020i009p01209

41. Tsang, Y.W., Tsang, C.F.: Hydrological characterization of variable-aperture fractures, In: Barton and Stephansson (eds.) Rock Joints, pp. 423-431, Blkema, Rotterdam (1990)
42. Tsang, Y.W., Witherspoon, P.A.: Hydromechanical behavior of a deformable rock fracture subject to normal stress. J. Geophys. Res. 86(B10), 9287-9298 (1981). https://doi.org/10.1029/JB086iB10p09287
43. Tzelepis, V., Moutsopoulos, K.N., Papaspyros, J.N.E., Tsihrintzis, V.A.: Experimental investigation of flow behavior in smooth and rough artificial fractures. J. Hydrol. 521, 108-118 (2015). https://doi.org/10.1016/j.jhydrol.2014.11.054
44. Unger, A.J.A., Mase, C.W.: Numerical study of the hydro- mechanical behavior of two rough fracture surfaces in contact. Water Resour. Res. 29(7), 2101-2114 (1993). https://doi.org/10.1029/93WR0051
45. Yeo, I.W., De Fremitas, M.H., Zimmerman, R.W.: Effect of shear displacement on the aperture and permeability of a rock fracture. Int. J. Rock Mech. Min. Sci. Geomech. Abstr. 35 (8), 1051-1070 (1998). https://doi.org/10.1016/S0148-9062(98)00165-X
46. Watanabe, K., Takahashi, H.: Fractal geometry characterization of geothermal reservoir fracture networks. J. Geophys. Res. Solid Earth (1978-2012) 100(B1), 521-528 (1995). https://doi.org/10.1029/94JB02167
47. Wilson, C.R., Witherspoon, P.A.: Flow interference effects at fracture intersections. Water Resour. Res. 12(1), 102-104 (1976). https://doi.org/10.1029 /WR012i001p00102
48. Witherspoon, P.A., Wang, J.S.Y., Iwai, K., Gale, J.E.: Validity of cubic law for fluid flow in a deformable rock fracture. Water Resour. Res. 16(6), 1016–1024 (1980). https://doi.org/10.1029/WR016i006p01016
49. Zimmerman, R.W., Bodvarsson, G.S.: Hydraulic conductivity of rock fractures. Transport Porous Med. 23, 1-30 (1996). https://doi.org/10.1007/BF00145263
50. Zimmerman, R.W., Yeo, I.W.: Fluid flow in rock fractures: From the Navier-Stokes equations to the cubic law, in Dynamics of Fluids in Fractured Rock. Geophys. Monogr. 122, edited by B. Faybishenko, P. Witherspoon, and S. Benson, 213–224, AGU, Washington, D.C. (2000)
51. Zimmerman, R.W., Kumar, S., Bodvarsson, G.S.: Lubrication theory analysis of the permeability of rough-walled fractures. Int. J. Rock Mech. Min. Sci. Geomech. Abstr. 28, 325-331 (1991). https://doi.org/10.1016/0148-9062(91)90597-F